# Wideband Characterization of Equatorial Ionospheric Fading Using MUOS Signals

Subash, Joeal; Cannon, Paul S.

*DOI:*
10.1029/2022RS007457



*Document Version*
Publisher's PDF, also known as Version of record

*Citation for published version (Harvard):*
Subash, J & Cannon, PS 2022, 'Wideband Characterization of Equatorial Ionospheric Fading Using MUOS Signals', *Radio Science*, vol. 57, no. 8, e2022RS007457. https://doi.org/10.1029/2022RS007457

Radio Science

RESEARCH ARTICLE
10.1029/2022RS007457

# Wideband Characterization of Equatorial Ionospheric Fading Using MUOS Signals

**Joeal Subash**[1] and **Paul S. Cannon**[1]

[1]Space Environment and Radio Engineering (SERENE), University of Birmingham, Birmingham, UK

**Key Points:**

- Fading close to the Fresnel frequency is well correlated over greater bandwidths than higher frequency fading components
- Over all fading frequencies, flat fading is far more common than frequency selective fading, for signal bandwidths less than 15 MHz
- Flat fading is the dominant fading mechanism for high VHF and low UHF equatorial satellite communication systems

**Correspondence to:**
P. S. Cannon,
p.cannon@bham.ac.uk

**Citation:**
Subash, J., & Cannon, P. S. (2022). Wideband characterization of equatorial ionospheric fading using MUOS signals. *Radio Science*, *57*, e2022RS007457. https://doi.org/10.1029/2022RS007457

Received 6 MAR 2022
Accepted 28 JUL 2022

**Author Contributions:**
**Conceptualization:** Paul S. Cannon
**Data curation:** Joeal Subash
**Formal analysis:** Joeal Subash
**Funding acquisition:** Paul S. Cannon
**Investigation:** Joeal Subash
**Methodology:** Paul S. Cannon
**Project Administration:** Paul S. Cannon
**Resources:** Paul S. Cannon
**Software:** Joeal Subash
**Supervision:** Paul S. Cannon
**Validation:** Joeal Subash
**Writing – original draft:** Paul S. Cannon
**Writing – review & editing:** Joeal Subash, Paul S. Cannon



**Abstract** Six hundred hours of data from a receiver located at the Cape Verde Atmospheric Observatory at 15°N (dip latitude), has been used to explore the fading correlation of 300–360 MHz trans-ionospheric signals from the MUOS satellite. Using these data, we have highlighted that the inter-frequency correlation varies with the fading frequency; components at frequencies close to the Fresnel frequency tend to be well correlated over bandwidths between 15 MHz and greater than 20 MHz, but those at higher fading frequencies are only well correlated over bandwidths between 0.1 and 5 MHz at a correlation threshold of 0.7. When considered over all fading frequencies, flat fading is far more common than frequency selective fading, such that when the frequency separation is 5 MHz and when $S_4$ lies between 0.7 and 0.8, the ratio is ∼16:1, when the separation is 10 MHz the ratio is ∼9:1 and when the separation is 15 MHz it is ∼7:1. Together, the results in this paper suggest that flat fading is the dominant fading mechanism for satellite communication systems, with bandwidths up to 15 MHz, operating in the high VHF and low UHF bands in the equatorial region. At still higher operating bandwidths we expect frequency selective fading to become dominant as the differentially delayed multipath components, occurring via Fresnel scale irregularities, cause destructive and constructive interference.

## 1. Introduction

To varying extents, the ionosphere affects all trans-ionospheric radio frequency (RF) communications, surveillance and navigation systems operating at frequencies below ∼2 GHz (Cannon, 2009). At ultra-high frequencies (UHF, 300–3000 MHz) trans-ionospheric communication and radar systems are highly affected by the ionosphere with impacts that can be mitigated or indeed made worse by the radio system design. These ionospheric effects are most prevalent at high and low latitudes where the time-varying irregularities, which cause scattering of the signals, cause rapid phase and amplitude variations of the signal (scintillation). The climatology of scintillation is well understood (e.g.,Aarons, 1993; Basu et al., 1988) with equatorial scintillation, which is studied in this paper, most prevalent in the period between sunset and local midnight.

It would probably be fair to say that the vast majority of the scintillation impact studies have addressed UHF radar and surveillance systems (e.g.,Belcher et al., 2017; Mannix et al., 2017; Xu et al., 2004) and L-band GNSS navigation systems (e.g.,Hapgood et al., 2021; Hernández-Pajares et al., 2011; Kintner et al., 2007). Much less emphasis has been placed on the effects of scintillation on trans-ionospheric UHF communications systems.

Early studies at frequencies appropriate to V/UHF communication systems by Whitney et al. (1972) and Whitney and Basu (1977) explored the characteristics of amplitude scintillation on 137 and 360 MHz communications channels, finding that the channel can be described by a Nakagami-m distribution such that when the scintillation is intense, $m = 1$ and the distribution is Rayleigh. More recently, Chen et al. (2022) have suggested the use of other models. A widely used index to describe amplitude scintillation is $S_4$, being the root-mean-square of the power $P$ divided by the average power, $\overline{P}$ (Briggs & Parkin, 1963) and this will be used extensively in this paper:

$$S_4 = \frac{\left[\sum \left(P - \overline{P}\right)^2\right]^{0.5}}{\overline{P}} \quad (1)$$

Much of the early literature focused on the narrowband channel but some looked at how the channel varied between separated narrowband frequencies. For example, Fremouw et al. (1978) used coherent Wideband Satellite signal transmissions to show that the UHF coherency bandwidth can be as low as 11.5 MHz. More recently, Knepp and Houpis (1992) and later Cannon et al. (2006) used the ALTAIR VHF and UHF radars, located on

Kwajalein Island (9.4°N, 166.8°E) to estimate the channel scattering function and thereby the coherency time and bandwidth. In both cases signals were reflected from calibration spheres in low earth orbit. Cannon et al. (2006) reported that during a period when the two-way $S_4$ index was above 0.8, the median coherency bandwidths were 0.8 and 2.1 MHz at 158 and 422 MHz, respectively—much less than the one way values measured by Fremouw et al. (1978). Johnson and Taagholt (1985) experimentally explored the consequences of fade depth on both low and high latitude communications paths. Further understanding of the channel and what it tells us about the ionospheric irregularities has also been gained through propagation modeling using, for example, thin phase screen, parabolic equation approaches, see Knepp (1983a), Knepp (1983b), and Rogers et al. (2009).

These and other papers have formed the basis for the design and modeling of the United States Department of Defense (DoD) Mobile User Objective System (Kullstam & Keskinen, 2000; Satorius & Zhong, 2003; Zhong & Satorius, 2003).

This paper seeks to extend our understanding of the communications propagation channel and especially the wideband channel. In particular, it seeks to quantify the UHF coherency bandwidth associated with equatorial scintillation, its probability of occurrence and whether the associated amplitude fading is flat or frequency selective.

## 2. The Experiment

### 2.1. Wideband Transmissions

The results reported herein are based on transmissions from the MUOS-3 satellite located at ∼15.5°W. MUOS is a wideband UHF geosynchronous satellite communications system with a 20 MHz downlink bandwidth consisting of four 5 MHz wideband code division multiple access (CDMA) channels centered on 370 MHz. The transmission bandwidth is comparable to the 18 MHz employed by Cannon et al. (2006) and the fixed geometry to geosynchronous orbit is particularly advantageous for long term monitoring. However, the MUOS CDMA spreading codes and even the modulation are unpublished and this has restricted our measurements to those of the signal power only.

### 2.2. The Cape Verde Islands Receiving System

To capture the signal, wideband receiving equipment was operated at the Cape Verde Atmospheric Observatory (CVAO) located at 16.8°N, 24.8°W geographic, 10°N dip latitude, which is close to the peak of the equatorial scintillation region (Aarons, 1982). The MUOS satellite was visible at an elevation angle of 65°–71°, at an azimuth of 148°–152° but the antenna was pointed to the zenith. The system was operated (apart from minor outages) between 20 UT (Universal Time) and 02 UT each day from 16 December 2018 to 30 April 2019 resulting in 600 hr of data.

The receiving system consisted of a helical antenna with a gain of 14.8 dBi, a preamplifier with 21.5 dB gain and high and low pass filters with −3 dB points lying at 360 and 440 MHz. The signal was fed to a software defined radio tuned to 370 MHz with a 20 MHz bandwidth and a 14-bit analog to digital converter (90 dB dynamic range). Data were stored on a 24 TByte disc array. The data were $I$, $Q$ sampled at 20 MHz (50 ns) per channel resulting in ∼4 TByte of data per night which were decimated by a factor of 1,000. This involved taking 2,000 sample blocks, each lasting 100 μs, which were Fourier transformed (by FFT) to generate a 20 MHz power spectrum with a spectral resolution of 10 kHz. A thousand such power spectra were then averaged and the result stored every 0.1 s. Figure 1 depicts one such spectrum during a no scintillation period. The four 5 MHz multiplexes are marked, M1, M2, M3 and M4. The signal power associated with M1 is less than the others because of a high pass filter with a 3 dB point at 360 MHz. Superposed on the multiplexes are narrowband 25 kHz transmissions, for example, at ∼378 MHz.

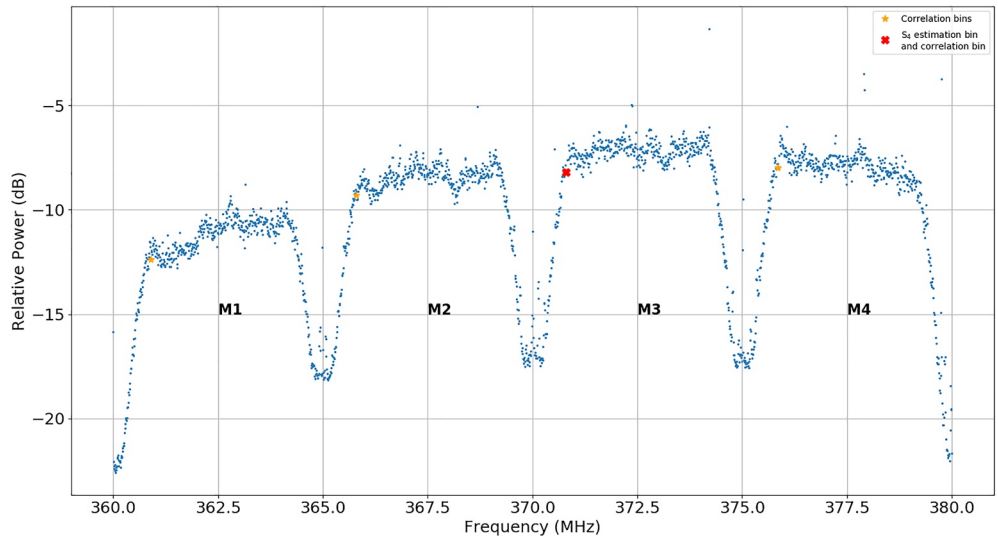


**Figure 1.** Received MUOS signal power, at 10 kHz resolution, averaged over 0.1 s during a period without scintillation (21 March 2019, starting at 21:15:02 UT).

## 3. Data Overview

Figure 2 summarizes the data and describes the observed probability distribution, in 15-min time bins for times between 2000 UT (~1820 LT) and 0200 UT (~0020 LT). (Local time (LT) is estimated from the longitude of the receiving station as this is a good approximation to the pierce point given the high elevation angle of the satellite relative to the receiver.)

In the figure, ten contiguous 10 kHz spectral bins from the lower frequency shoulder of multiplex M3 (Figure 1) were averaged and the $S_4$ calculated over 60 s. No detrending (high pass) filter was used apart from that imposed

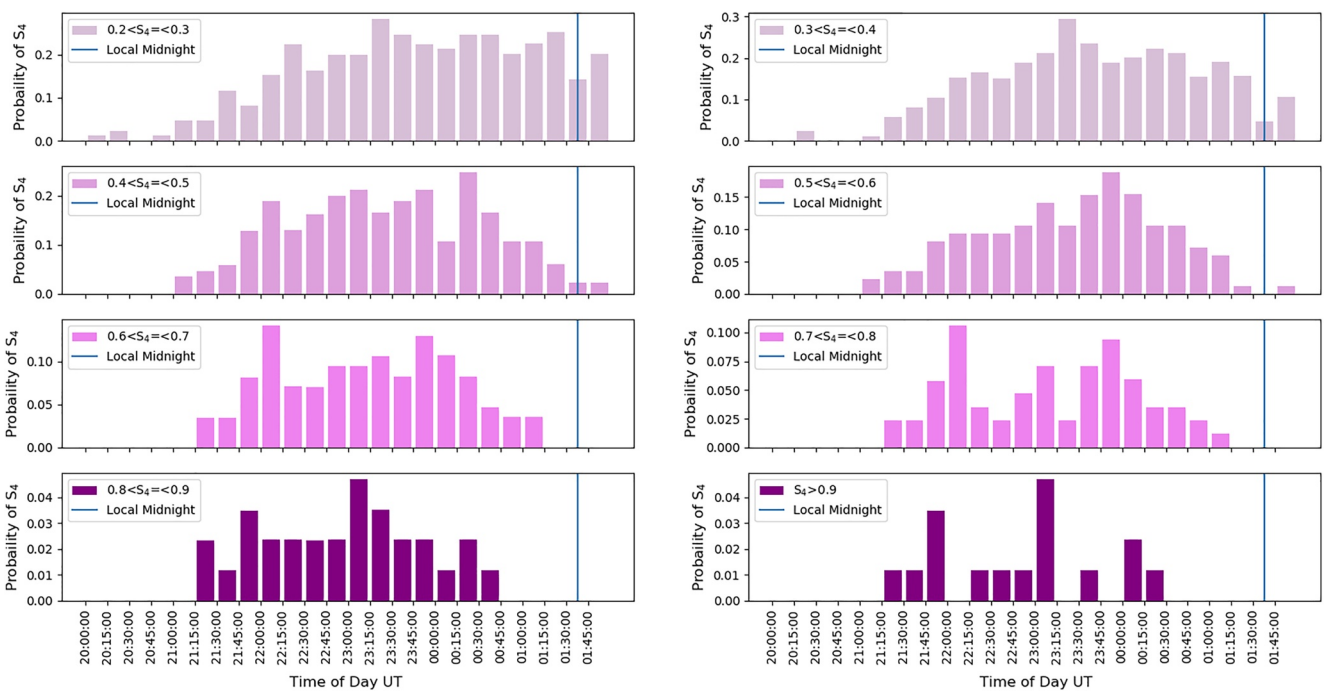


**Figure 2.** Probability of scintillation in $S_4$ bands as a function of UT, for the period 16 December 2018–30 April 2019 at Cape Verde Atmospheric Observatory. The time bins are 15 min.

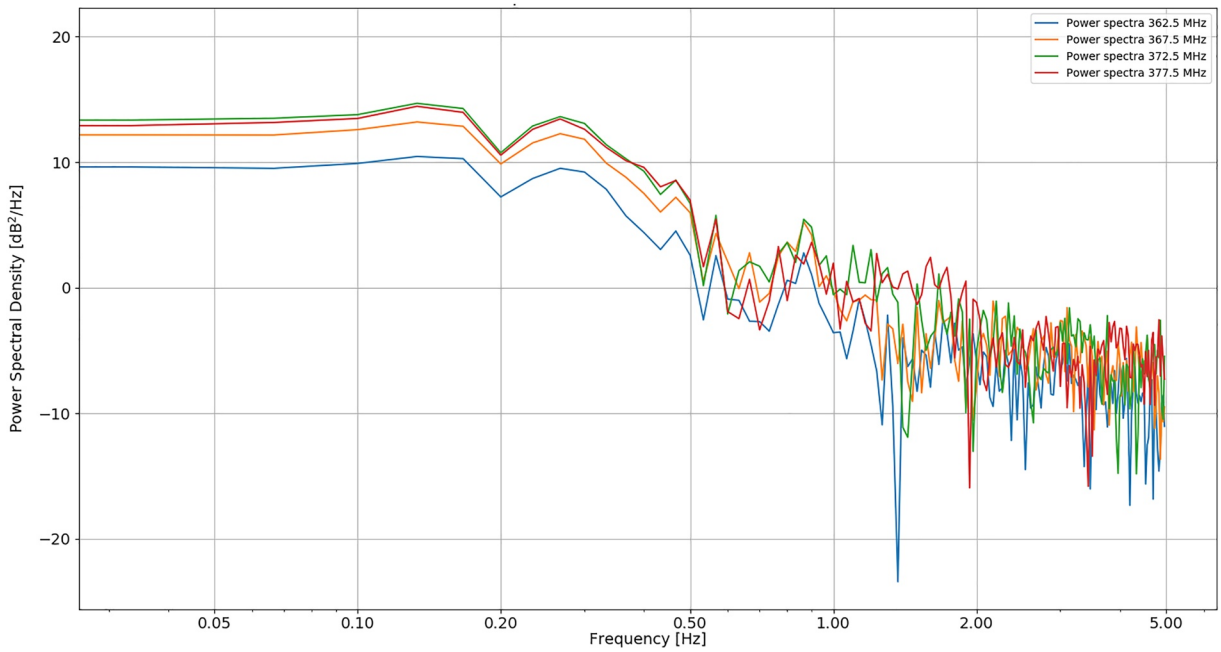


**Figure 3.** Flat fading: 30 s average, power spectral density of each multiplex, (21 March 2019, starting at 21:19:01 UT) when $S_4(30\text{ s}) = 1.06$.

by the averaging period. The shoulder, rather than the center of the multiplex, was chosen to minimize the impact of narrowband transmissions and the impact of the latter were further minimized by averaging across the 10 bins (100 kHz). As we will see, the correlation bandwidths are greater than 100 kHz and averaging across 10 bins is, therefore, a valid approach.

The expected activity between sunset and midnight local time (denoted by a vertical blue line) is apparent, with stronger events occurring at earlier times. Of the 36,000 min of data collected at CVAO during the measurement period, only 60 min exhibited $S_4 > 0.8$ and only 14 min exhibited $S_4 > 0.9$. This was a very inactive period at the bottom of the sunspot cycle.

## 4. Fading Comparisons Over 20 MHz

Figure 3 presents the fading power spectral densities at the specified multiplex frequencies corresponding to a 30 s period when $S_4$ averaged over 30 s (or more concisely $S_4(30\text{ s})$) was close to unity. As already noted, the recorded signal associated with the lowest frequency multiplex (M1) is less than the other three.

The Fresnel frequency, above which the signal exhibits a power law decay with frequency provides a useful reference value on such plots. The Fresnel scale, $d_F$ for a path through the ionosphere from a geostationary satellite is (Bhattacharyya et al., 2000):

$$d_F = \sqrt{2\lambda z} \tag{2}$$

Here $\lambda$ is the signal wavelength and $z$ is the altitude of the $F$-region irregularities, which are assumed to lie in a narrow phase screen. If $v$ is the horizontal drift velocity of the irregularities, then the Fresnel frequency $\upsilon_F$ is given by:

$$\upsilon_F = \frac{v}{d_F} \tag{3}$$

Both $v$ and $d_F$ are variable within any 1 day and from day-to-day. For illustrative purposes, we assume that the F-region irregularities lay at an altitude of 350 km. The ionospheric plasma drift velocity could have ranged from magnetically quiet time values of ∼200 $\text{ms}^{-1}$ (Bhattacharyya et al., 2001) to active time values between 300 and 500 $\text{ms}^{-1}$ (Aarons, 1982) and in highly active periods may have reached 1000 $\text{ms}^{-1}$ (Basu et al., 1999). Adopting

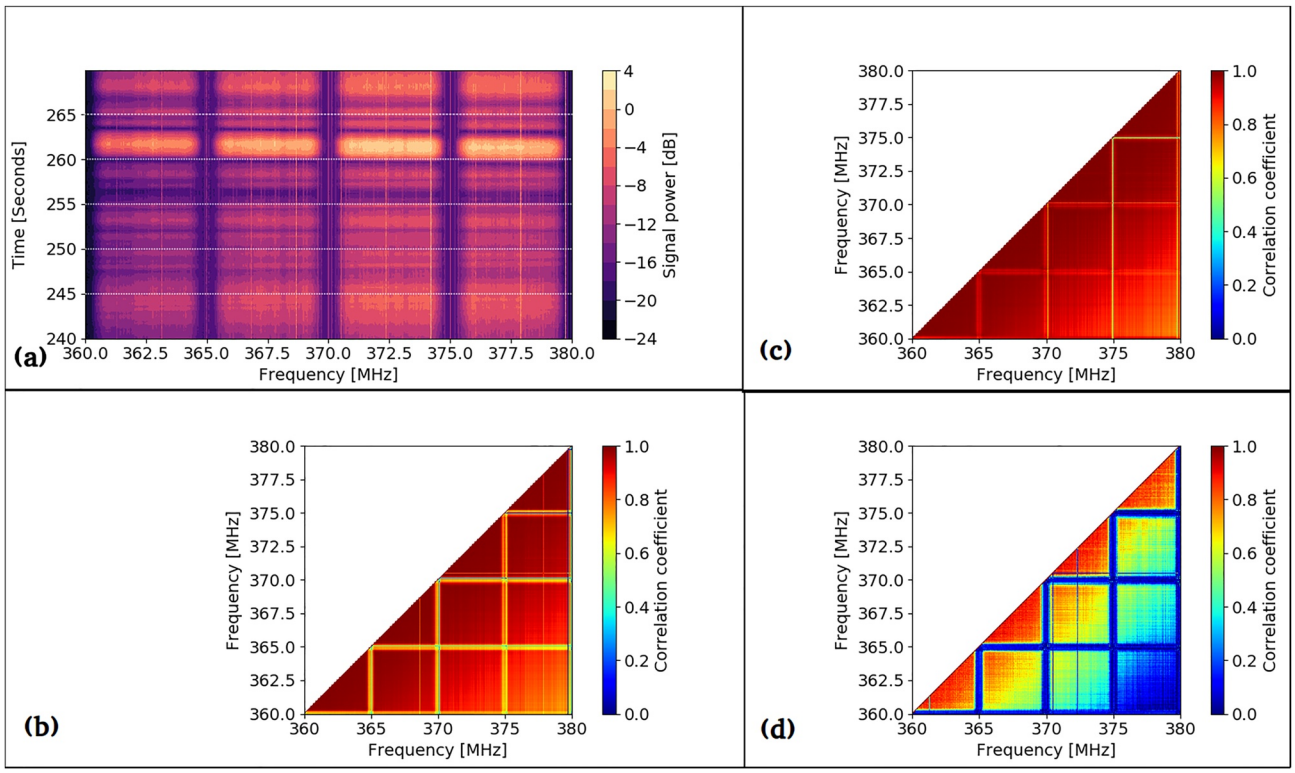


**Figure 4.** (a) Radio frequency power spectrum of the MUOS signal (21 March 2019, starting at 21:19:01 UT) when $S_4(30\text{ s}) = 1.06$. (b), (c) and (d) show Pearson's correlation coefficient across the MUOS spectrum. (b) unfiltered, (c) 0.7 Hz low pass filtered and (d) 0.7 Hz high pass filtered; frequency resolution 10 kHz.

a active time value of 400 $ms^{-1}$ realises a Fresnel frequency of 0.54 Hz which scales proportionally at lower and higher velocities.

In this active period example, at frequencies below and immediately above the estimated Fresnel frequency the power spectra variations are very similar on all multiplexes with a ~3 dB drop at 0.2 Hz which will be seen as a slow fade in the time domain. Similar and deeper nulls are common in the data for frequencies between ~0.2 and 0.5 Hz which suggests that simple two ray (or at least a small number of rays) interference often remains stable over the averaging period of 30 s. At higher frequencies, where diffraction from multiple irregularities dominates, the spectra (signals) are increasingly uncorrelated. Note that in our experiment there is negligible impact from ground-reflection multipath because the receiver antenna points close to zenith.

Figure 4a shows the time domain variation in signal power over the same 30 s of data, and across the full 20 MHz. Early on the fades are well synchronized across the full 20 MHz, signifying flat fading, but the strong fade at ~262 s occurs first on the high frequency multiplex and ~0.5 s later on the low frequency multiplex. In other words, at this time we have strong frequency selective fading.

Figure 4b takes the analysis a step further by examining the fading correlation between all of the RF frequency components from the perspective of Pearson's correlation coefficient, $R$. By inspection, we can see that, averaged over 30 s, the channel is flat out to 20 MHz except in the narrow bands at the 5 MHz channel boundaries, as indicated by the high (>0.7) correlation. However, the slowly increasing decorrelation suggests that the correlation bandwidth is probably not much higher. As we might expect from the preceding discussion, the high power, low frequency (0.7 Hz, 30 dB per octave low pass filtered) components are likewise well correlated over 20 MHz (Figure 4c) but the low power, high frequency (0.7 Hz, 30 dB per octave high pass filtered) components are highly decorrelated (Figure 4d). In the latter case, the correlation bandwidth is, by inspection, only ~5 MHz (at $R = 0.7$) across the full experimental bandwidth except in the vicinity of the guard bands. Although not shown here, when the high-pass filter break point is increased to 1.1 Hz the correlation bandwidth decreases to 3 MHz.

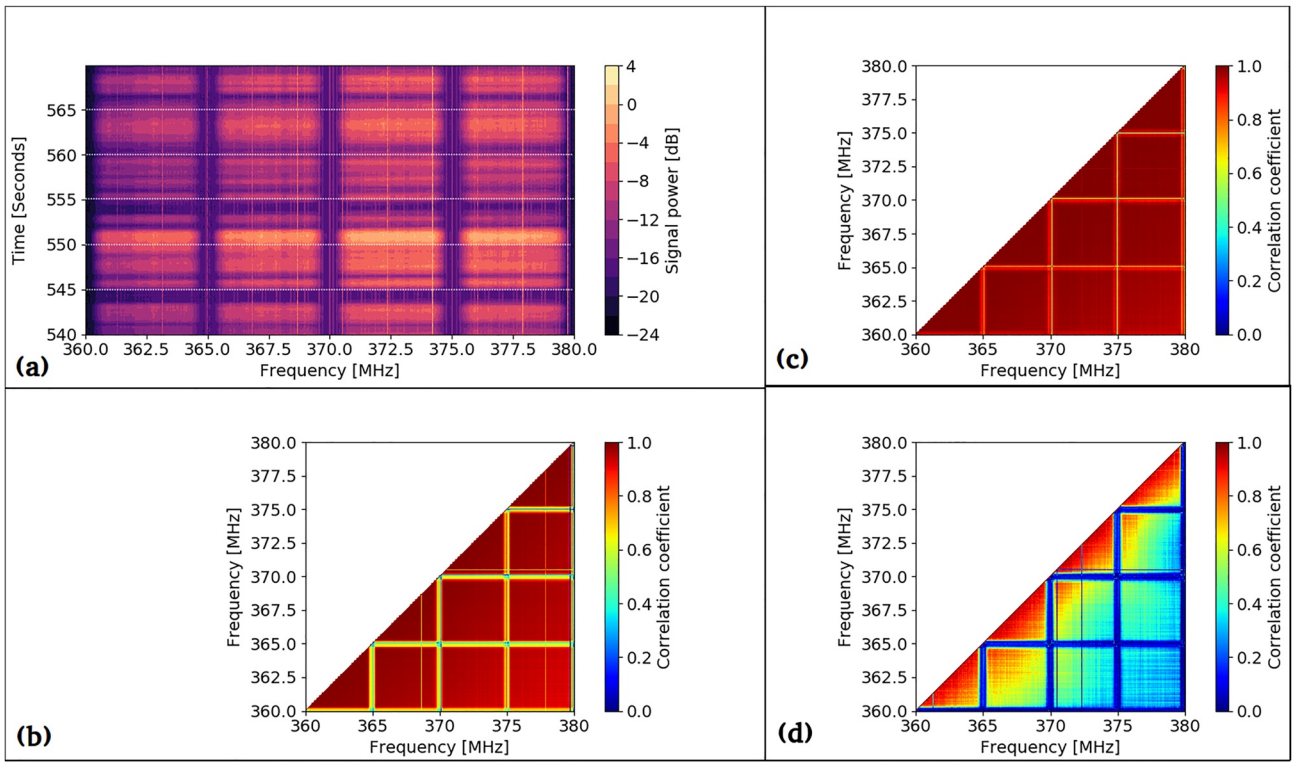


**Figure 5.** (a) Radio frequency power spectrum of the MUOS signal 21 March 2019, starting at 21:24:01 UT when $S_4(30\ s) = 0.87$. (b), (c) and (d) show Pearson's correlation coefficient across the MUOS spectrum, (b) unfiltered, (c) 0.7 Hz low pass filtered and (d) 0.7 Hz high pass filtered; frequency resolution 10 kHz.

Figure 5 and Figure 6 provide further examples when the $S_4(30\ s)$ is lower, at 0.87 and 0.54 respectively. Again panels (a) suggest that flat fading predominates and again panels (b) suggest that the overall fading correlation bandwidth is often >20 MHz, built up of highly coherent low frequency components (panels (c)) and less coherent high frequency components (panels (d)) with correlation bandwidths of ∼4.5 and ∼2 MHz.

Figure 7, Figure 8 and Figure 9 re-examine these three periods in more detail by breaking each 30 s period into four 7.5 s sub-periods. The differential fading delays between the different multiplexes are now much more obvious and the dynamics of the correlation bandwidth are apparent.

The correlation bandwidths of MUOS transmissions for all fading frequencies, only the low frequency components and only the high frequency components were visually estimated for 38 cases when $S_4$ was above 0.4. In all cases the unfiltered and low pass filtered correlations lay between 15 and >20 MHz measured at a correlation coefficient of 0.7. The high pass filtered correlation bandwidths varied greatly and lay between 0.1 and 5 MHz, again measured at a correlation threshold of 0.7. In all cases, the overall correlation bandwidth was dominated by the strong, slow frequency fading and not by the weak, high frequency scintillation.

No dependency of correlation bandwidth on $S_4$ could be discerned for the case of all fading frequencies, low pass components or high pass components. Inspection of the data revealed that the correlation bandwidth of the high pass components is dependent on the cut-off frequency of the HPF relative to the Fresnel frequency. In particular, when $S_4$ is high, the drift velocity is likely to be high and the Fresnel frequency may be comparable to 0.7 Hz or even higher. Consequently, during active periods the high-power fading components below and close to the Fresnel frequency will contaminate estimates of the correlation bandwidth associated with the low-power higher frequency scintillating signals.

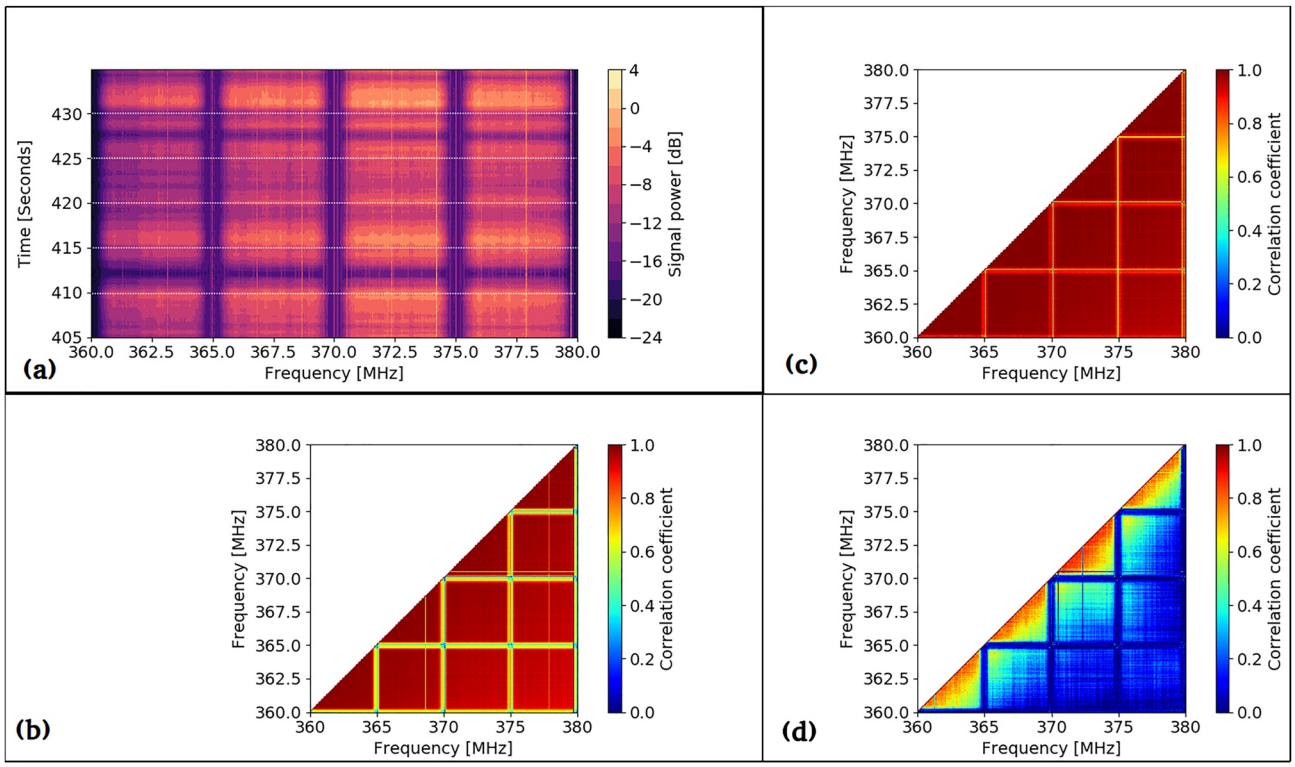


**Figure 6.** (a) Radio frequency power spectrum of the MUOS signal 21 March 2019, starting at 21:21:46 UT when $S_4(30) = 0.54$. (b), (c) and (d) show Pearson's correlation coefficient across the MUOS spectrum, (b) unfiltered, (c) 0.7 Hz low pass filtered and (d) 0.7 Hz high pass filtered; frequency resolution 10 kHz.

## 5. Probability of Flat and Frequency Selective Fading

While studies, such as those discussed in Section 4, of coherency bandwidth are informative, the modem designer also needs to know how often flat fading (FF) or frequency selective fading (FSF) occurs. Only with that knowledge can the appropriate trade-offs be made to maximize the quality of service. CVAO data from the period 16 December 2018 to 30 April 2019, collected between 20 UT (1830 LT) and 02 UT (0030 LT) each day was available to determine these probabilities, however, given the quantity of data an automatic categorization technique was required.

The data were first pre-processed to calculate the signal magnitude with 10 Hz sampling resolution, from each of the four multiplexes M1, M2, M3 and M4 (respectively 360–365, 365–370, 370–375 and 375–380 MHz). In order to reduce the impact of noise, twenty 10 kHz spectral bins were incoherently averaged centered on 361.1, 366.1, 371.1 and 376.1 MHz (see Figure 1). These frequencies were chosen to be distant both from the nulls between multiplexes and the narrowband signals.

The categorization approach was based on the unnormalized correlation of the demeaned time series from two multiplexes. (The more conventional normalized correlation was not used because noise and the underlying modulation generated spurious correlations). If the unnormalized correlation of the two demeaned time-series is $R[n]$, then:

$$R[n] = \sum_{L=0}^{l} M_x[L+n]\, M_y[L+n] \tag{4}$$

where, $M_x$ and $M_y$ are the demeaned time series, $l$ is the correlation sample length and $n$ is the lag, which is set to zero. Correlations were calculated every 0.1 s and after some optimization the correlation sample length was set to eight (0.8 s) which is comparable to the duration of a deep fade.

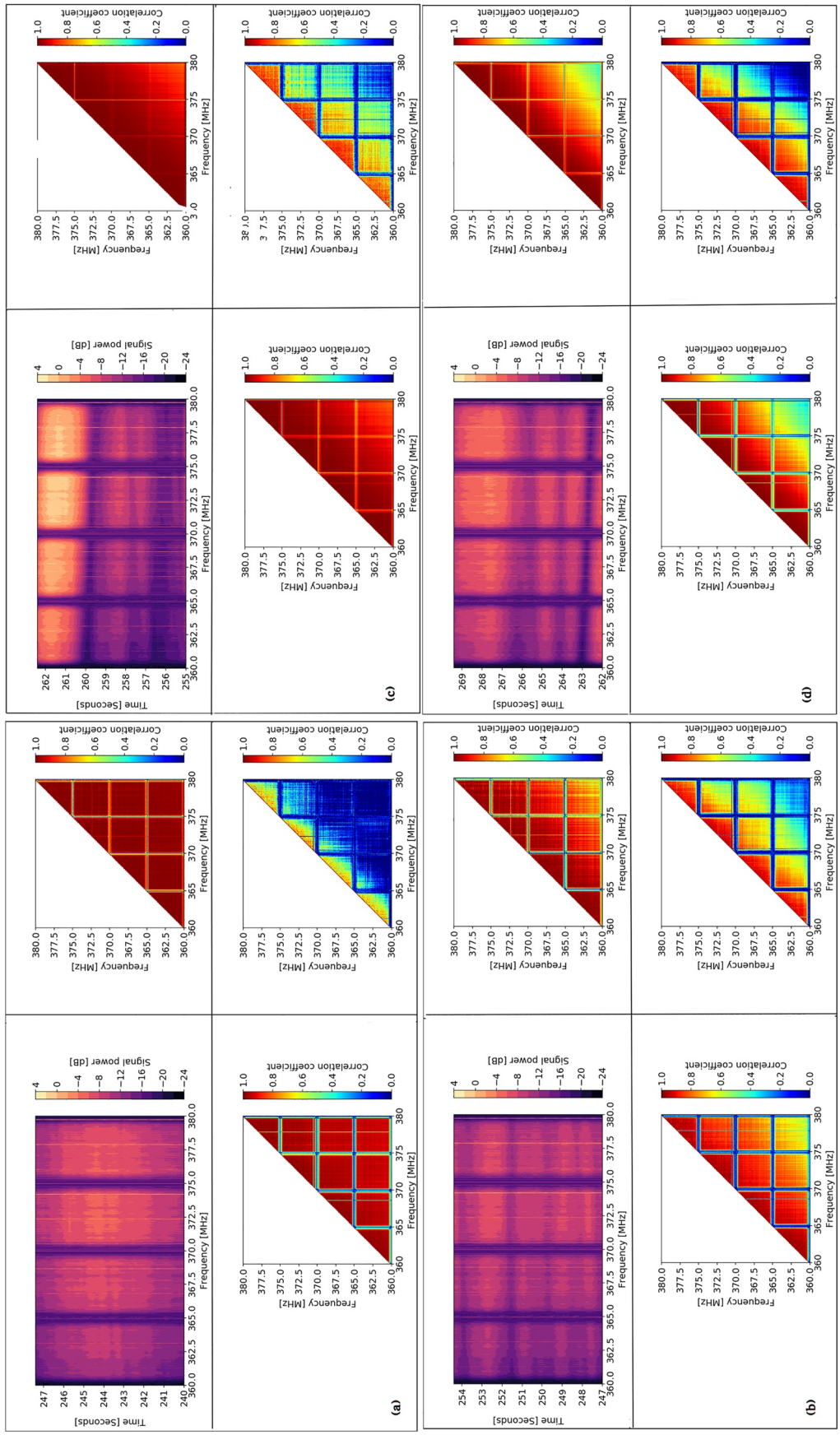


**Figure 7.** 21 March 2019, starting at 21:19:01 UT when $S_4 \sim 1.06$. Each panel (a), (b), (c) and (d) shows the 7.5s dynamic spectra (top-left), the Pearson correlation coefficient when data is unfiltered (bottom-left), filtered with a 0.7 Hz LPF (top-right) and filtered with a 0.7 Hz HPF (bottom-right). Total time across the four panels is 30 s.

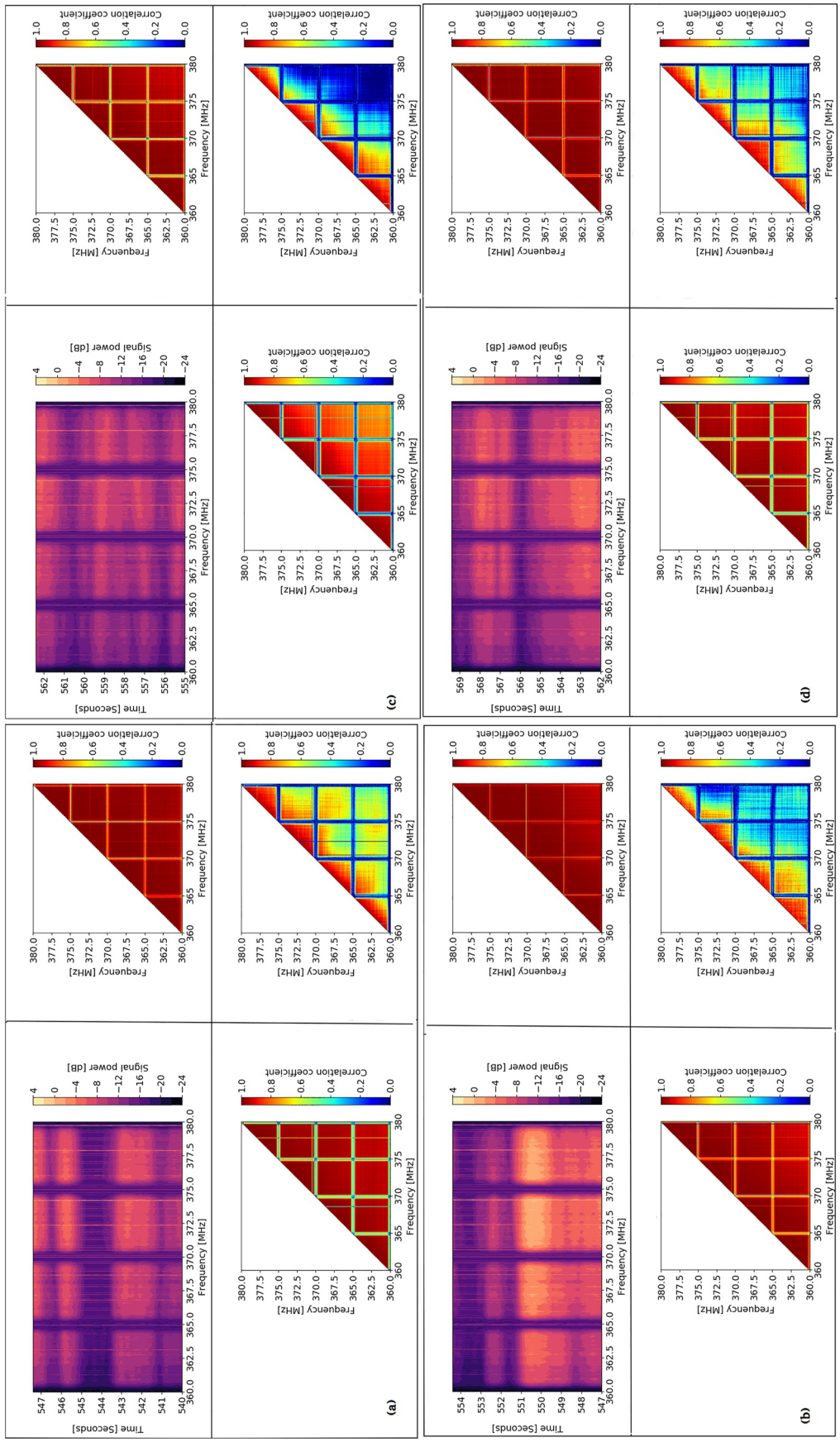


**Figure 8.** 21 March 2019, starting at 21:24:01 UT when $S_4 \sim 0.8$. Each panel (a), (b), (c) and (d) shows the 7.5 s dynamic spectra (a), the Pearson correlation coefficient when data is unfiltered (a), filtered with a 0.7 Hz LPF (c) and filtered with a 0.7 Hz HPF (d). Total time across the four panels is 30 s.

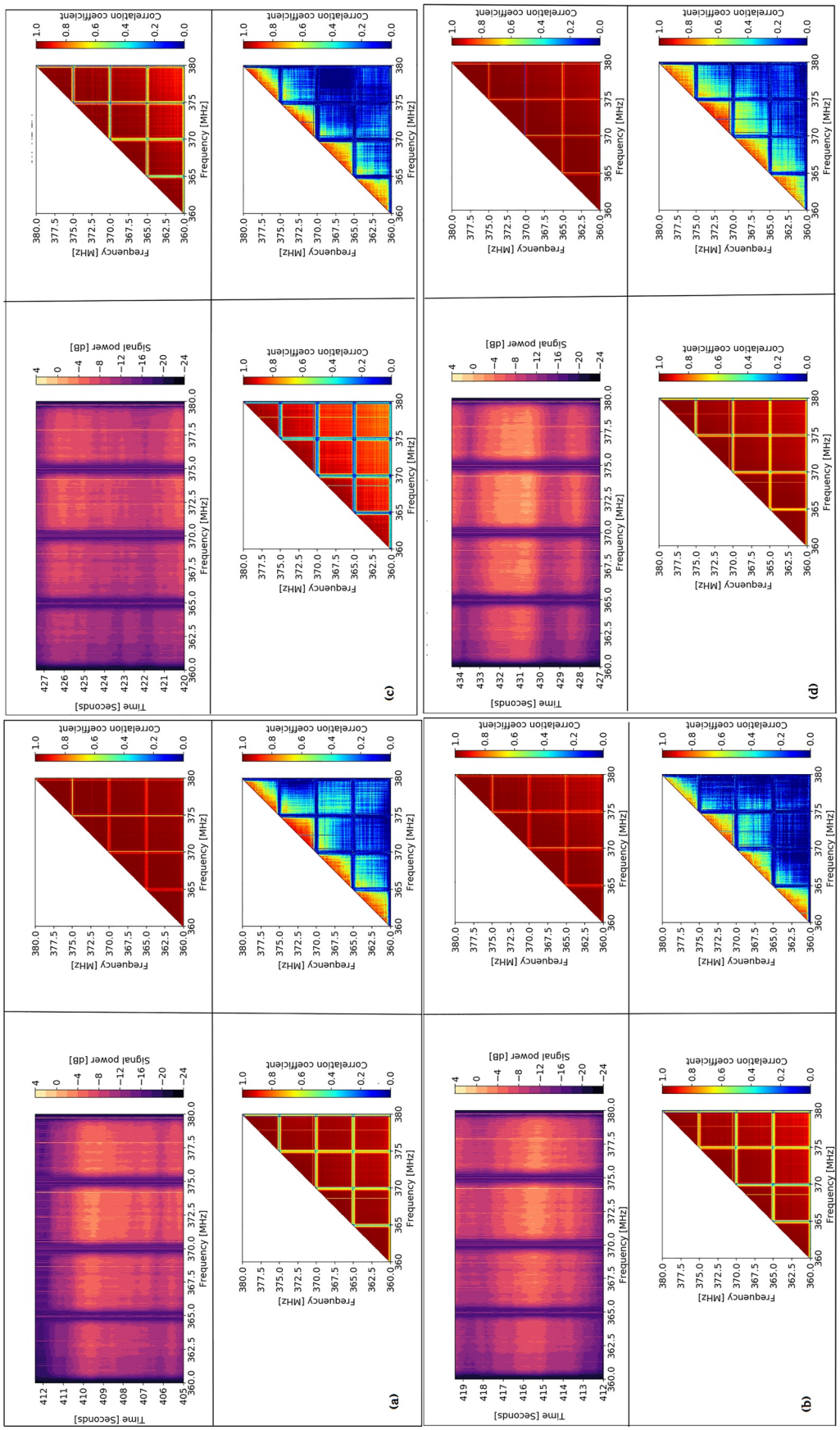


**Figure 9.** 21 March 2019, starting at 21:21:46 UT when $S_4 \sim 0.54$. Each panel (a), (b), (c) and (d) shows the 7.5 s dynamic spectra (a), the Pearson correlation coefficient when data is unfiltered (b), filtered with a 0.7 Hz LPF (c) and filtered with a 0.7 Hz HPF (d). Total time across the four panels is 30 s.

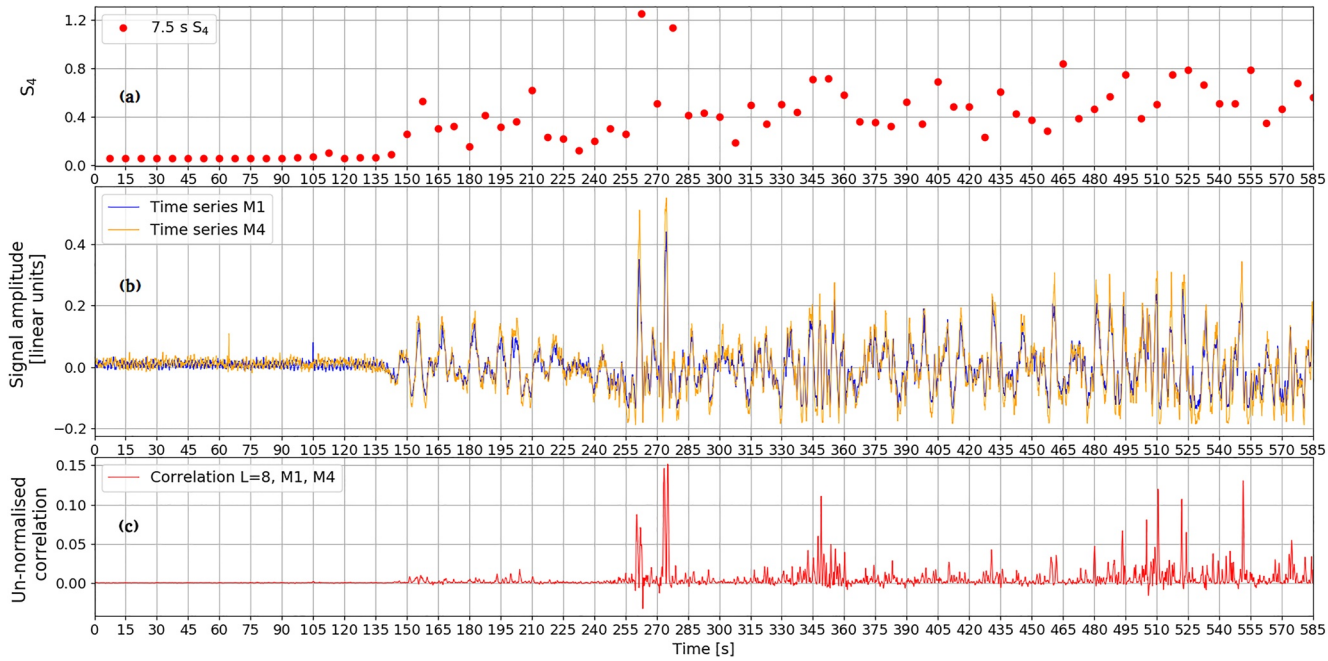


**Figure 10.** $S_4$(7.5 s) (a), M1 and M4 signal amplitude (b), $R$[0] (c).

If there is no noise or residual modulation on the signal, $R$[0] is positive if the signal variations are correlated (FF), is negative if the variations are anti-correlated (FSF) and is zero if the there is no fading (NF). To compensate for the noise and modulation NF cases were initially identified to have occurred when the correlation fell within a band of values close to zero. However, this three way categorization was unsuccessful, so only periods with significant levels of fading ($S_4 > 0.4$), where we could be confident of either FF or FSF fading, have been analyzed in this study.

Figure 10 shows 585 s of data to illustrate the effectiveness of this automatic processing, where the top panel (a) illustrates the time series of $S_4$(7.5 s), the middle panel (b) shows the signal power variations from the identified frequencies in M1 and M4 and the bottom panel (c), shows the correlation, $R$[0]. For example, between 150 and 255 s $S_4$(7.5 s) lies between 0.2 and 0.5. (The use of a 7.5 s average is of course far too short to give an accurate estimate of $S_4$ but provides a useful illustrative metric of the depth of fading). In panel (b) the signals are seen to be varying coherently during this period. This is confirmed in panel (c) where the correlation is largely positive indicating that the fading should be categorized as flat. Between 255 and 285 s $S_4$(7.5 s) increases to ∼1 and the signal variations are more intense. Now the correlations are both positive (FF) and negative (FSF). Figure 11, where the time axis has been expanded and an additional panel (d) added to show the fading decision, shows this more clearly. Inspection of these figures suggests that the algorithm is categorizing the data successfully.

In order to better understand the data, and also to further assess the FF and FSF categorization technique the data have been binned into $S_4$ bands calculated over 7.5 s, to provide a qualitative description of the prevailing fading. Within that 7.5 s the event durations are then appropriately distributed to FF or FSF with a 0.1 s resolution. (Note that the more usual 60 and 30 s averaging periods smoothed the data too much, but again we note that an $S_4$ calculated over just 7.5 s can only be expected to loosely describe the fading.) The number of 7.5 s blocks in each $S_4$ band are given above each column, and the number of events (points) in each panel are given in red. Only $S_4 > 0.4$ data is plotted to minimize the time with no fading because we are unable to categorize these periods. Events with durations above 7.5 s are aggregated and plotted in the 7.5 s bin. The analysis shows that the flat fading events are both more prevalent (numbers in red) and last longer, sometimes even exceeding 7.5 s. In contrast frequency selective fading events exhibit a short durations.

Figure 13 extends this analysis to determine the probability of FF or FSF occurring as a function of $S_4$(7.5 s) and frequency separation. Whilst Figure 12 only examined the number of events, Figure 13 weights the probability by the event durations. Again note that the short period $S_4$ calculation blurs the relationship with $S_4$, but it is very

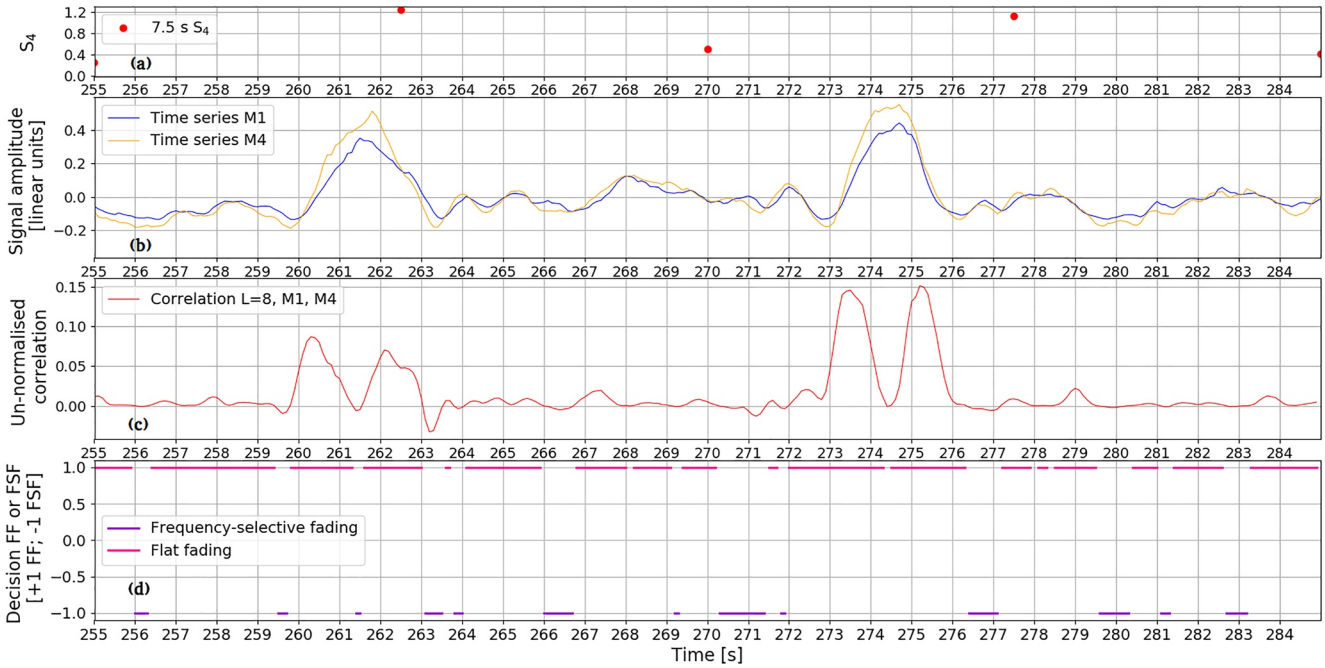


**Figure 11.** Excerpt starting at 255 s; $S_4$(7.5 s) (a), M1 and M4 signal amplitude (b), $R$[0] (c), fading decision (d).

clear that FF is much more likely to be experienced than FSF at all values of $S_4$ and that this becomes more likely as $S_4$ increases. Moreover, and as might be expected, as the frequency separation is reduced FF becomes even more prevalent. Figure 14 presents the ratio of FF to FSF for frequency separations of 5, 10 and 15 MHz as a function of $S_4$(7.5 s). For each frequency separation the ratio increases with increasing $S_4$.

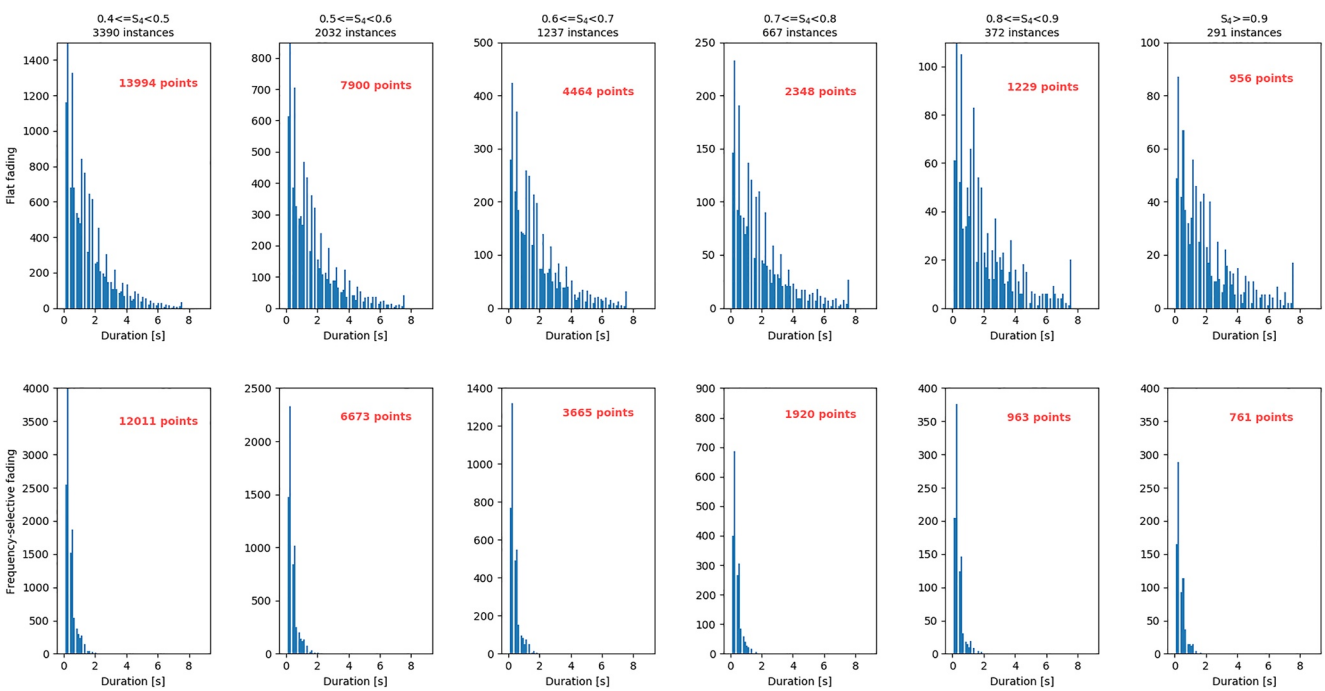


**Figure 12.** Number of instances of FF (top row) and frequency selective fading (bottom row) as a function of duration in different $S_4$ ranges when the frequency separation is 15 MHz (between 361.1 and 376.1 MHz) for the period between 20 UT and 01 UT.

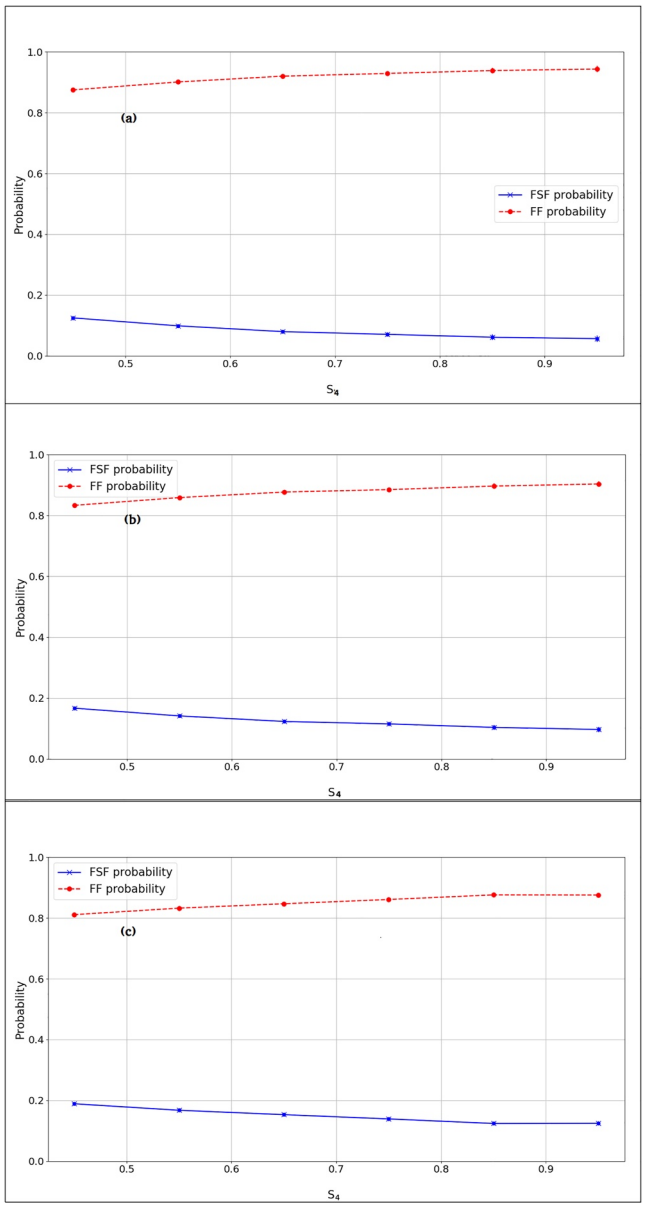


**Figure 13.** Probability of flat fading and frequency selective fading as a function of $S_4$(7.5 s) when the signal separation is 5 MHz (panel a), 10 MHz (panel b) and 15 MHz (panel c).

## 6. Discussion

CVAO lies at a geographic latitude of 16.8°N and at a dip latitude of 10°N and is ideally placed, relative to the equatorial F-region crest at 15°N (dip latitude), to measure ionospheric scintillation. However, the crest density and, therefore, the intensity of scintillation is strongly dependent on solar activity and during this experiment the smoothed sunspot number was very low varying between 4.3 and 6. Consequently, the anomaly was weak and little strong scintillation was monitored. Notwithstanding the low solar activity, examples of scintillation at all levels of $S_4$ occurred. Six hundred hours of data from CVAO has been used to explore the fading correlation of 300 MHz trans-ionospheric signals from the MUOS satellite.

In Figures 4–9 we have highlighted that the inter-frequency correlation varies with the fading frequency; signal components at frequencies close to the Fresnel frequency tend to be well correlated over bandwidths between 15 MHz and greater than 20 MHz, but those at higher fading frequencies are only well correlated over bandwidths between 0.1 and 5 MHz at a correlation threshold of 0.7. The inverse power law reduction in fading power means that these lower power uncorrelated signals have little impact on communications modem performance. The low frequency fading correlation results are in broad agreement with those of Fremouw et al. (1978) who measured one-way correlation bandwidths of 11 MHz or above using the DNA Wideband Satellite.

Direct comparison of this experimental data with the two way experimental coherence bandwidths measurements reported by Knepp and Houpis (1992) and Cannon et al. (2006) who both reflected V/UHF ALTAIR radar signals from orbiting calibration spheres is not possible. These authors, measured much lower coherency bandwidths which could be attributed to the two way path. However, we also speculate that the detrending of the orbital radar measurements, which was necessary because the target was moving rapidly, may have filtered out of some of the correlated low frequency fading components.

To quantify which type of fading dominates, the data has also been searched to distinguish between periods of flat and frequency selective fading. When considered over all fading frequencies, flat fading is far more common than frequency selective fading, such that when the frequency separation is 5 MHz and when $S_4$ lies between 0.7 and 0.8, the ratio is ~16:1, when it is 10 MHz the ratio is ~9:1 and when it is 15 MHz it is ~7:1, see Figure 13 and Figure 14. The experiment was unable to resolve at what bandwidth frequency selective fading becomes more prevalent than flat fading, but the results suggest that this occurs above 30 MHz.

Figure 14 also indicates that the incidence of flat fading relative to frequency selective fading increases with $S_4$. At first sight this is counter intuitive, but is simply a consequence of flat fading events lasting longer at higher $S_4$, as identified in Figure 12. This trend suggests an increasing prevalence of relatively large irregularities, close to the Fresnel scale, causing refractive focusing and defocusing.

Together, the results in this paper suggest that flat fading is the dominant fading mechanism for satellite communication systems, with bandwidths up to 15 MHz, operating in the high VHF and low UHF bands in the equatorial region. The impact of the high frequency scintillation components, which could cause frequency selective fading is small because the components are both weak and short in duration. Their impact is seen through their superposition on the long, slow fades causing short periods of frequency selective fading. At still higher operating bandwidths (above those employed in the MUOS satellite) we expect frequency selective fading to eventually become dominant as the differentially delayed multipath components, occurring via Fresnel scale irregularities,

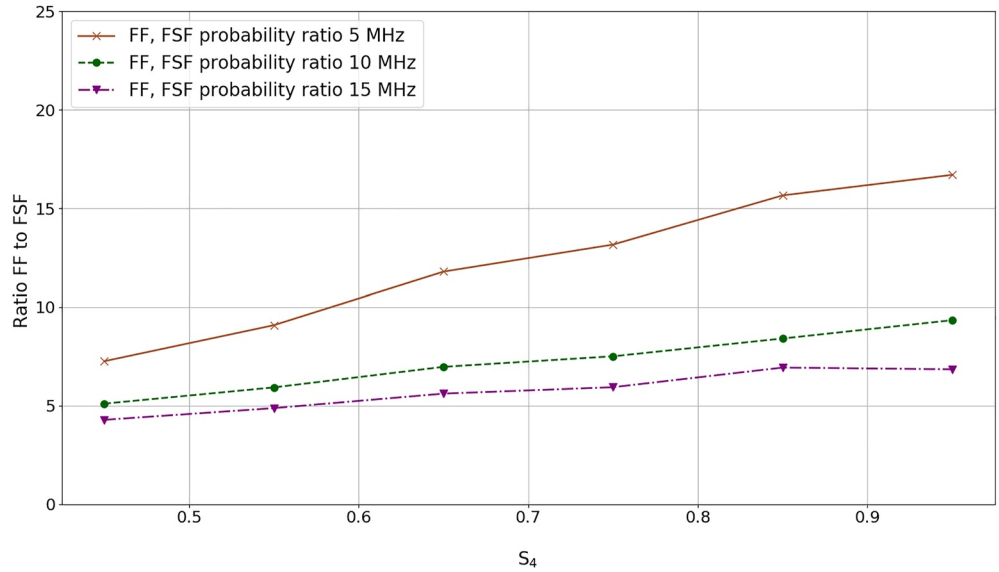


**Figure 14.** Ratio of flat fading to frequency selective fading at three bandwidths as a function of $S_4$(7.5 s).

results in destructive and constructive interference. Automatic gain control (AGC), which is effectively a low pass filter, will only exacerbate the tendency to flat fading.

## Data Availability Statement

The experimental data can be obtained at http://doi.org/10.5281/zenodo.6264201.

**Acknowledgments**
We acknowledge Matthew Angling for initiating this research and Enda McKenna and Stephen White for helping with the deployment and maintenance of the experiment. This work was supported by the Engineering and Physical Science Research Council (EPSRC) Grant No. EP/P008046/1.

## References

Aarons, J. (1982). Global morphology of ionospheric scintillation. *Proceedings of the IEEE*, *70*(4), 360–377. https://doi.org/10.1109/PROC.1982.12314

Aarons, J. (1993). The longitudinal morphology of equatorial *F*-layer irregularities relevant to their occurrence. *Space Science Reviews*, *63*(3), 209–243. https://doi.org/10.1007/BF00750769

Basu, S., Groves, K. M., Quinn, J. M., & Doherty, P. (1999). A comparison of TEC fluctuations and scintillations at Ascension Island. *Journal of Atmospheric and Solar-Terrestrial Physics*, *61*(16), 1219–1226. https://doi.org/10.1016/S1364-6826(99)00052-8

Basu, S., Mackenzie, E., & Basu, S. (1988). Ionospheric constraints on VHF/UHF communications links during solar maximum and minimum period. *Radio Science*, *23*(3), 363–378. https://doi.org/10.1029/RS023i003p00363

Belcher, D. P., Mannix, C. R., & Cannon, P. S. (2017). Measurement of the ionospheric scintillation parameter from SAR images of clutter. *IEEE Transactions on Geoscience and Remote Sensing*, *55*(10), 5937–5943. https://doi.org/10.1109/TGRS.2017.2717081

Bhattacharyya, A., Basu, S., Groves, K. M., Valladares, C. E., & Sheehan, R. (2001). Dynamics of equatorial *F* region irregularities from spaced receiver scintillation observations. *Geophysical Research Letters*, *28*(1), 119–122. https://doi.org/10.1029/2000GL012288

Bhattacharyya, A., Beach, T. L., Basu, S., & Kintner, P. M. (2000). Nighttime equatorial ionosphere: GPS scintillations and differential carrier phase fluctuations. *Radio Science*, *35*(1), 209–224. https://doi.org/10.1029/1999RS002213

Briggs, B. H., & Parkin, I. A. (1963). On the variation of radio star and satellite scintillations with zenith angle. *Journal of Atmospheric and Terrestrial Physics*, *25*(6), 339–366. https://doi.org/10.1016/0021-9169(63)90150-8

Cannon, P. S. (2009). Mitigation and exploitation of the ionosphere: A military perspective. *Radio Science*, *44*(1), RS0A20. https://doi.org/10.1029/2008RS004021

Cannon, P. S., Groves, K. M., Fraser, D. J., Donnelly, W. J., & Perrier, K. (2006). Signal distortion on V/UHF trans-ionospheric paths: First results from WIDE. *Radio Science*, *41*(5), RS5S40. https://doi.org/10.1029/2005RS003369

Chen, Z., Liu, Y., Guo, K., & Wang, J. (2022). Study of the ionospheric scintillation radio propagation characteristics with cosmic observations. *Remote Sensing*, *14*(3), 578. https://doi.org/10.3390/rs14030578

Fremouw, E. J., Leadabrand, R. L., Livingston, R. C., Cousins, M. D., Rino, C. L., Fair, B. C., & Long, R. A. (1978). Early results from the DNA Wideband satellite experiment-complex-signal scintillation. *Radio Science*, *13*(1), 167–187. https://doi.org/10.1029/RS013i001p00167

Hapgood, M., Angling, M. J., Attrill, G., Bisi, M., Cannon, P. S., Dyer, C., et al. (2021). Development of space weather reasonable worst-case scenarios for the UK national risk assessment. *Space Weather*, *19*(4). https://doi.org/10.1029/2020SW002593

Hernández-Pajares, M., Juan, J. M., Sanz, J., Aragón-Àngel, À., García-Rigo, A., Salazar, D., & Escudero, M. (2011). The ionosphere: Effects, GPS modeling and the benefits for space geodetic techniques. *Journal of Geodesy*, *85*(12), 887–907. https://doi.org/10.1007/s00190-011-0508-5

Johnson, A., & Taagholt, J. (1985). Ionospheric effects on C3I satellite systems in Greenland. *Radio Science*, *20*(3), 339–346. https://doi.org/10.1029/RS020i003p00339

Kintner, P. M., Ledvina, B. M., & de Paula, E. R. (2007). GPS and ionospheric scintillation. *Space Weather*, *5*(9). https://doi.org/10.1029/2006SW000260

Knepp, D. L. (1983a). Analytical solution for the two-frequency mutual coherence function for spherical wave propagation. *Radio Science*, *18*(4), 535–549. https://doi.org/10.1029/RS018i004p00535

Knepp, D. L. (1983b). Multiple phase-screen calculation of the temporal behavior of stochastic waves. *Proceedings of the IEEE*, *71*(5), 722–737. https://doi.org/10.1109/PROC.1983.12660

Knepp, D. L., & Houpis, H. L. F. (1992). Kwajalein 1988 propagation effects experiment assessment and results, Defense Nuclear Agency, (DNA-TR-91-180).

Kullstam, P. A., & Keskinen, M. J. (2000). Ionospheric scintillation effects on UHF satellite communications. In *Paper presented at the MILCOM 2000 proceedings. 21st century military communications. Architectures and technologies for information superiority*, (vol. 2, pp.779–783). https://doi.org/10.1109/MILCOM.2000.904036

Mannix, C. R., Belcher, D. P., & Cannon, P. S. (2017). Measurement of ionospheric scintillation parameters from SAR images using corner reflectors. *IEEE Transactions on Geoscience and Remote Sensing*, *55*(12), 6695–6702. https://doi.org/10.1109/TGRS.2017.2727319

Rogers, N. C., Cannon, P. S., & Groves, K. M. (2009). Measurements and simulation of ionospheric scattering on VHF and UHF radar signals: Channel scattering function. *Radio Science*, *44*(1), 1–10. https://doi.org/10.1029/2008rs004033

Satorius, E. H., & Zhong, Y. (2003). Channel modeling and simulation for mobile user objective system (MUOS)--Part II: Selective scintillation and terrestrial multipath fading. In *Paper presented at the IEEE international conference on communications, 2003*. ICC '03. https://doi.org/10.1109/ICC.2003.1204107

Whitney, H. E., Aarons, J., Allen, R. S., & Seemann, D. R. (1972). Estimation of the cumulative amplitude probability distribution function of ionospheric scintillations. *Radio Science*, *7*(12), 1095–1104. https://doi.org/10.1029/RS007i012p01095

Whitney, H. E., & Basu, S. (1977). The effect of ionospheric scintillation on VHF/UHF satellite communications. *Radio Science*, *12*(1), 123–133. https://doi.org/10.1029/RS012i001p00123

Xu, Z.-W., Wu, J., & Wu, Z.-S. (2004). A survey of ionospheric effects on space-based radar. *Waves in Random Media*, *14*(2), S189–S273. https://doi.org/10.1088/0959-7174/14/2/008

Zhong, Y., & Satorius, H. (2003). Channel modeling and simulation for mobile user objective system (MUOS)–part 1: Flat scintillation and fading. In *Paper presented at the IEEE international conference on communications, 2003*. Anchorage. https://doi.org/10.1109/ICC.2003.1204106. ICC '03.